Fig. 1
W: 103.5 mm
H: 89mm
(Full page width)

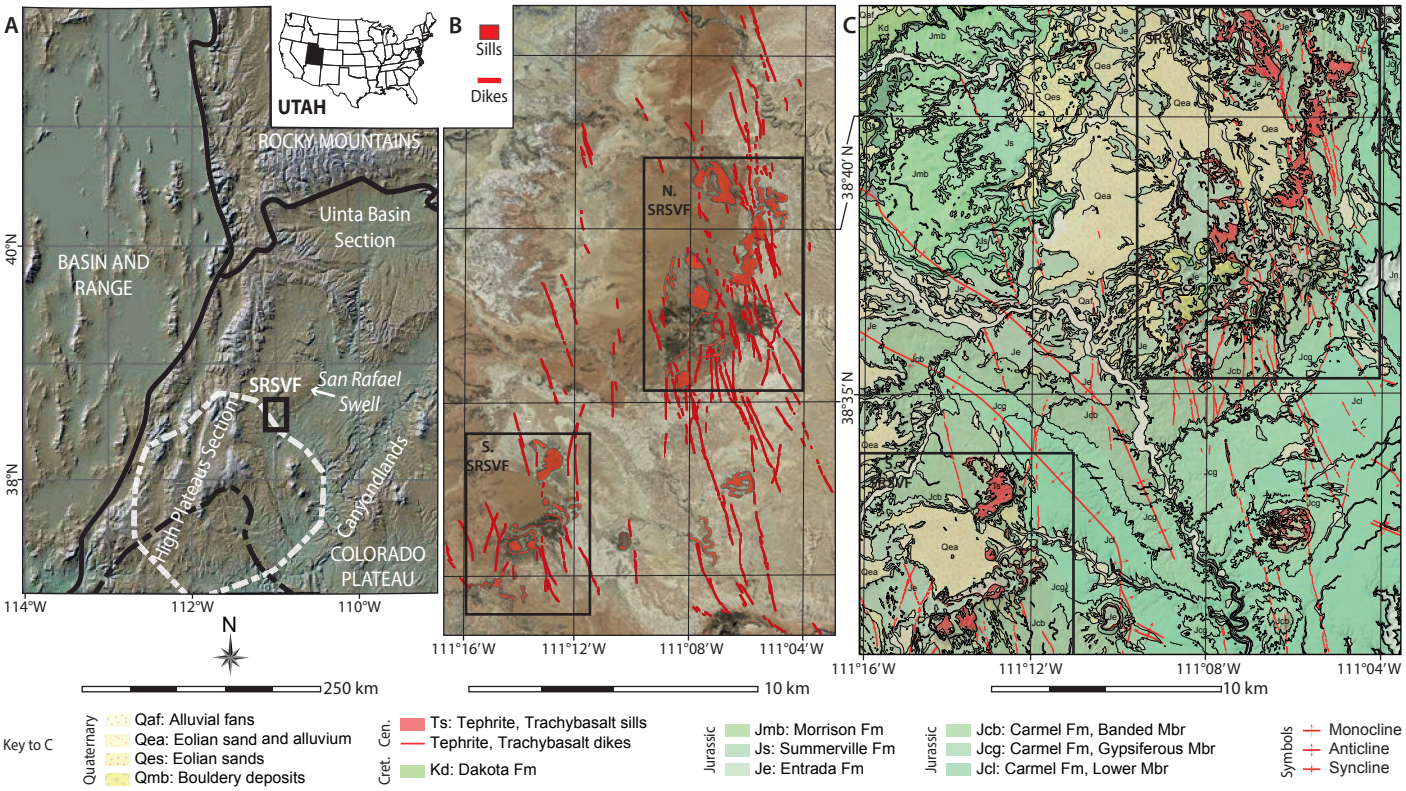

Fig. 1. Location maps for the San Rafael Sub-Volcanic Field in Utah. (A) Digital elevation Model for Utah, showing major structural and depositional areas of the Colorado Plateau. Solid black line shows province boundaries. Dashed black line is a region of lower-crustal delamination and crustal thinning detailed in Levander et al. (2011); dashed white line is their outline of a downwelling body at 200 km depth, estimated from body wave tomography. (B) Aerial imagery for the San Rafael Sub-Volcanic Field (SRSVF) highlighting location and distribution of intrusive bodies. (C) Geological map of the region of interest, showing relative positions of the Northern (N.) and Southern (S.) SRSVF. Cen.: Cenozoic. Cret.: Cretaceous. FM: Formation. Mbr: Member.

Fig. 2
W: 123 mm
H: 162 mm
(2-column width)

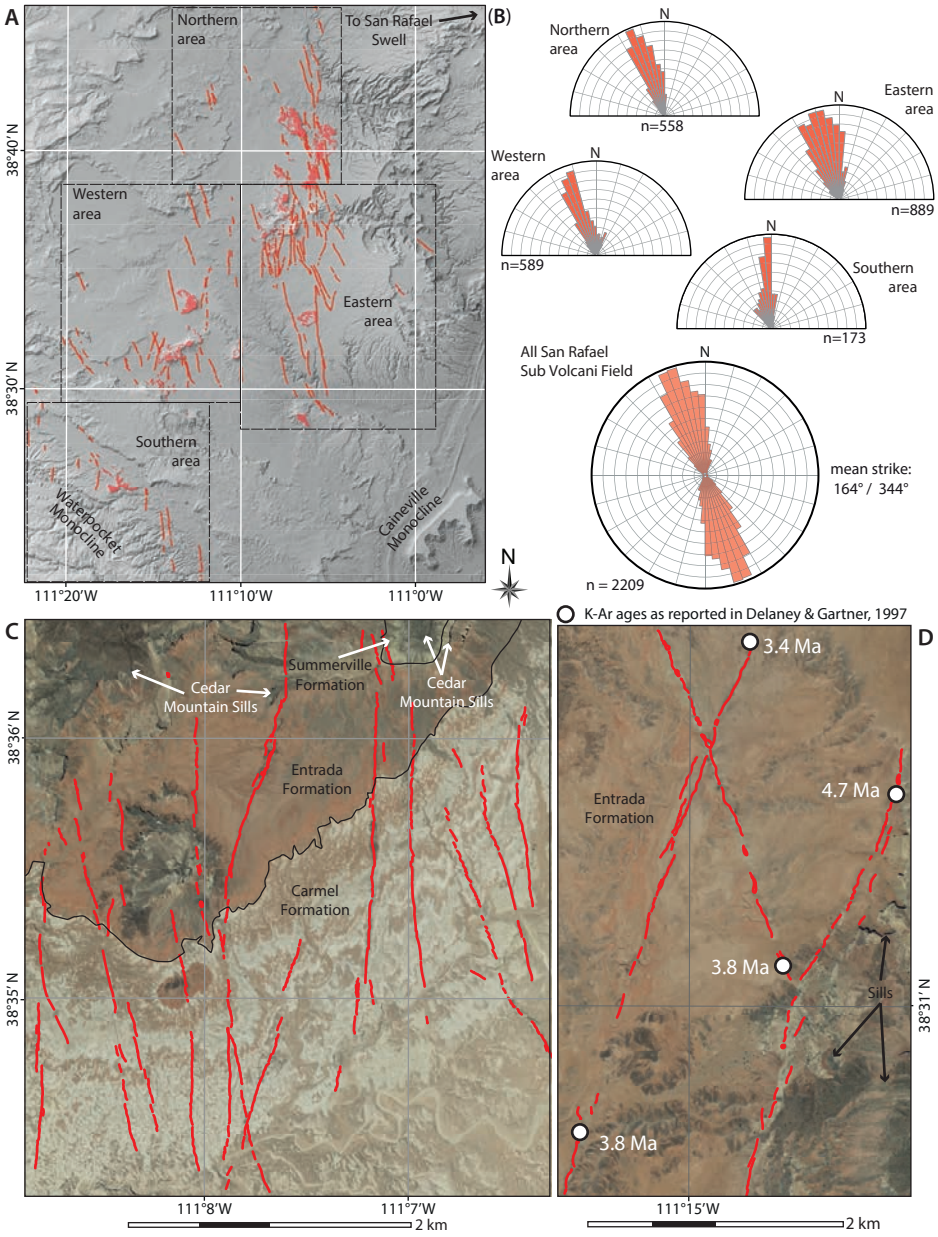

Fig. 2. Dike orientations in the SRSVF. (A) Hill shaded digital elevation model of the SRSVF showing dikes identified from aerial images. (B) Rose plots show dike orientations, separated by geographic location, and combined. Interpreted aerial image of dikes in (C) the eastern and (D) the western SRSVF showing the acute angular relationship between dike segments.

Fig. 3
W: 125 mm
H: 125 mm
(2-column width)

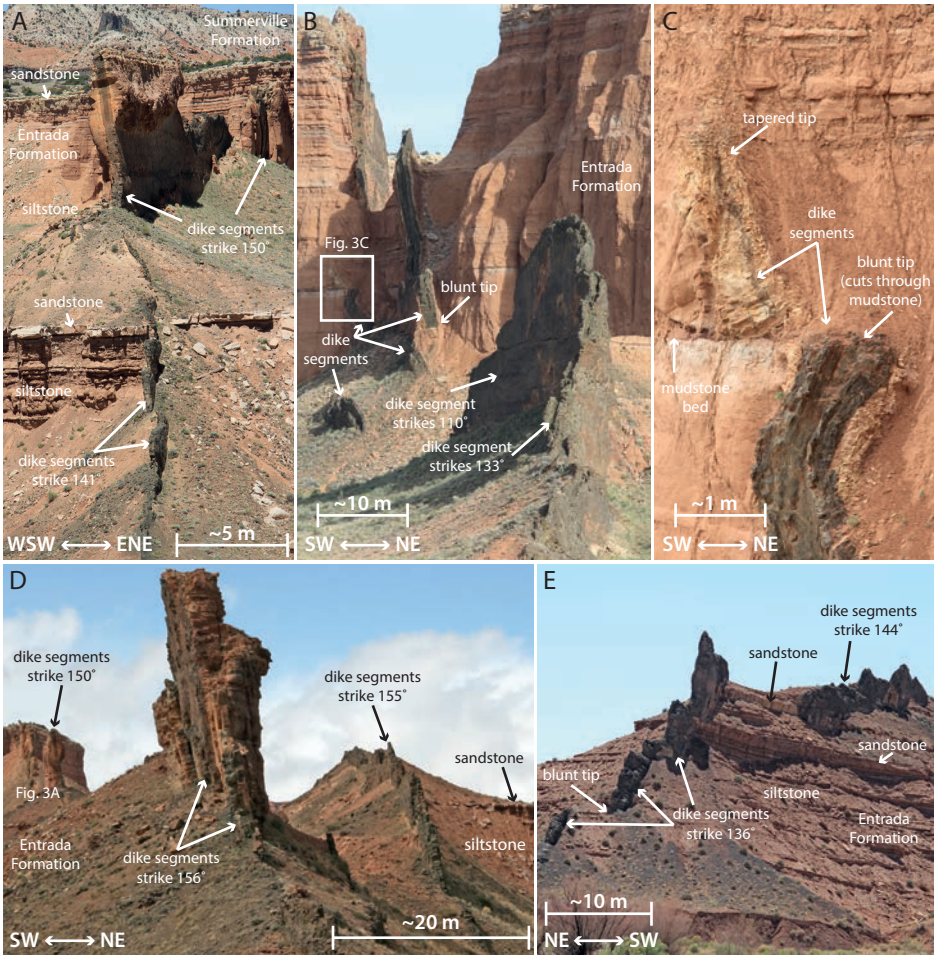

Fig. 3. Field photographs of dikes hosted in the Entrada Formation, within the SRSVF. (A) 1 m thick dike cuts sandstone-siltstone units, and shows minor angular deflection from vertical through the siltstone. (B) Segmented dikes show acute angular relationship (~23°) along strike. Segments both cut and abut a thin (10-30 cm thick) mudstone that separates siltstones above and below. (C) Dike segment abuts upper contact of a mudstone. Dike appears to be continuous across the mudstone, but shows a pronounced thinning above the contact, and ~1 m lateral offset. (D) Steeply-dipping dikes butting sandstones and siltstones. (D) Steeply-dipping dike segments show segmentation in plan, and section view. Segment tips correspond to unit boundaries in section view, but no pre-existing discontinuity is noted in plan view.

Fig. 4
W: 123 mm
H: 173 mm

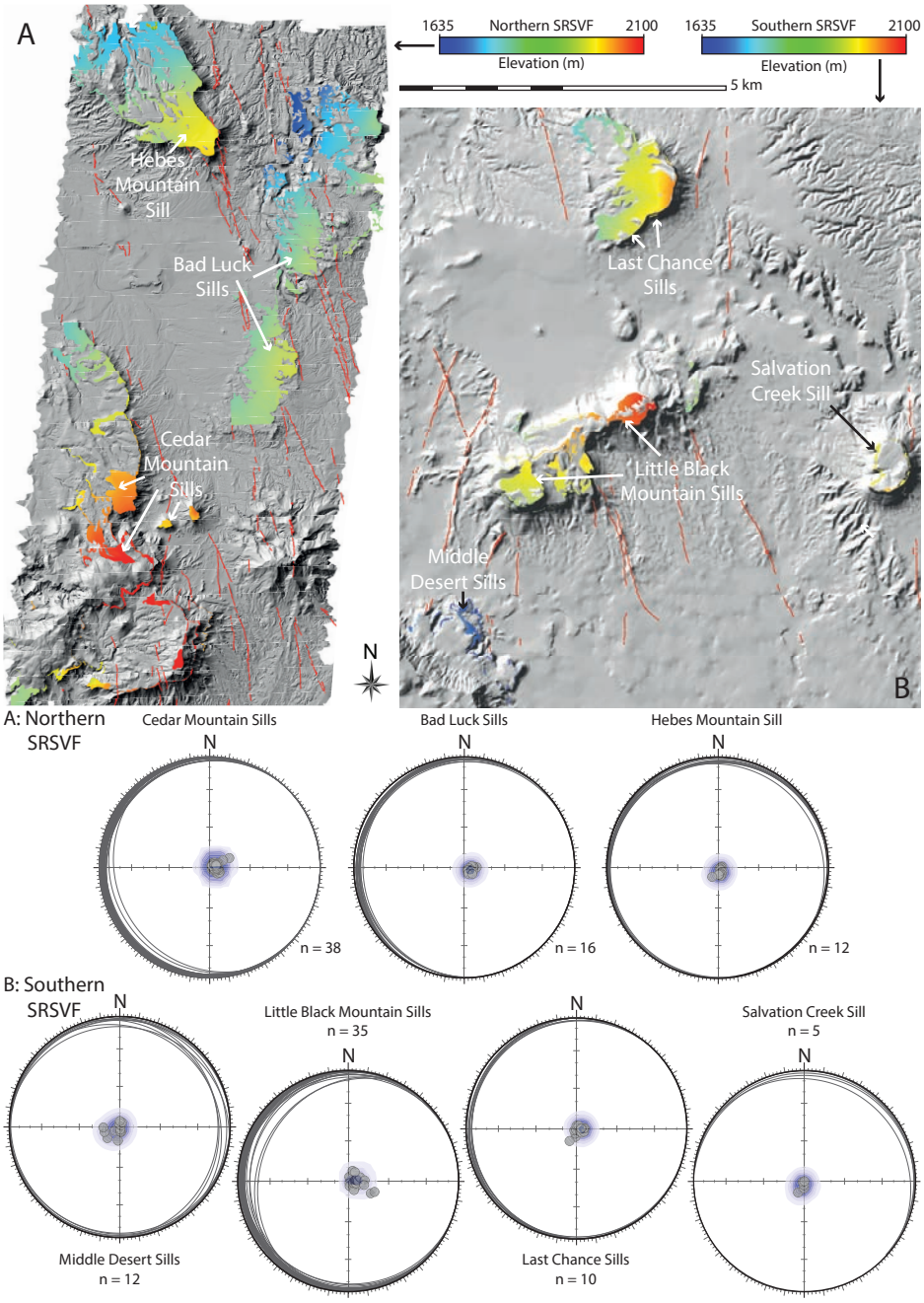

Fig. 4. Geometric analysis of thick sills in the SRSVF. Hillshaded digital elevation models for (A) the northern SRSVF and (B) the southern SRSVF. Models show extrapolated elevation data for sill top contacts. Lower hemisphere stereographic projections show sill top contact polygon attitudes as great circles, and contoured poles to planes for each sill system named in A and B. See text for details.

Fig. 5
w: 185 mm
H: 128 mm
(full page width)

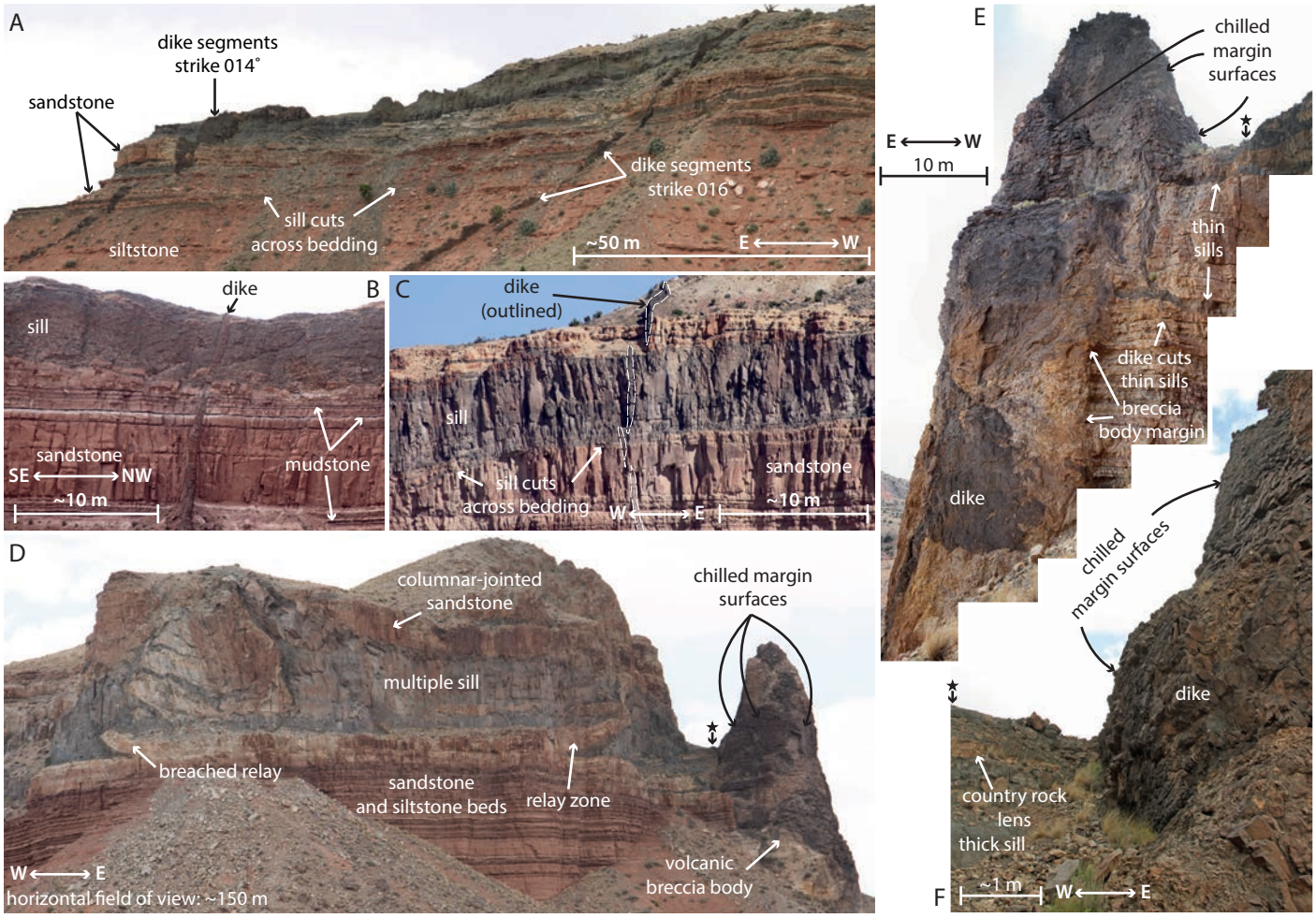

Fig. 5. Examples of cross-cutting relationships between sills and dikes. (A) Segmented dikes cut sills in the southern SRSVF. (B-C) Dikes cut sills in the northern SRSVF. Note that the thick sills in B and C are not parallel to bedding. Note that in C, dike segments (outlined with white dashes) cut the sill upper and lower contacts, but appear to abut internal sill contacts. (D-F) "Co-magmatic conduit of Richardson et al., (2015). Dikes within the volcanic breccia body (dark grey) cut thin sills below the main thick sill (light grey) shown in D. Chilled margin surfaces are observed at the same leval as the thick sill, though no direct contact is observed. Black star represents a marker to tie images D, E, and F.

Fig. 6
W: 185 mm
H: 197 mm
(Full page width)

Fig. 6. The Cedar mountain sills, northern SRSVF. (A) Photo panorama showing the Lower, Central, and Upper Cedar Mountain sills. (B-D) Dike and volcanic breccia body cut the Central Cedar Mountain sill. (C) Breccia body is developed along vertical joints in the sill. (D) Dike cuts volcanic breccia body, and shows chilled margin contacts with the Central Cedar Mountain sill. (E) Central Cedar Mountain sill is segmented across an apparent relay structure. Relay structure is brecciated, and hosts minor (cm-thick) sills that are inclined relative to the main sill.

Fig. 7
W: 225 mm
H: 112 mm
(2 column height, landscape)

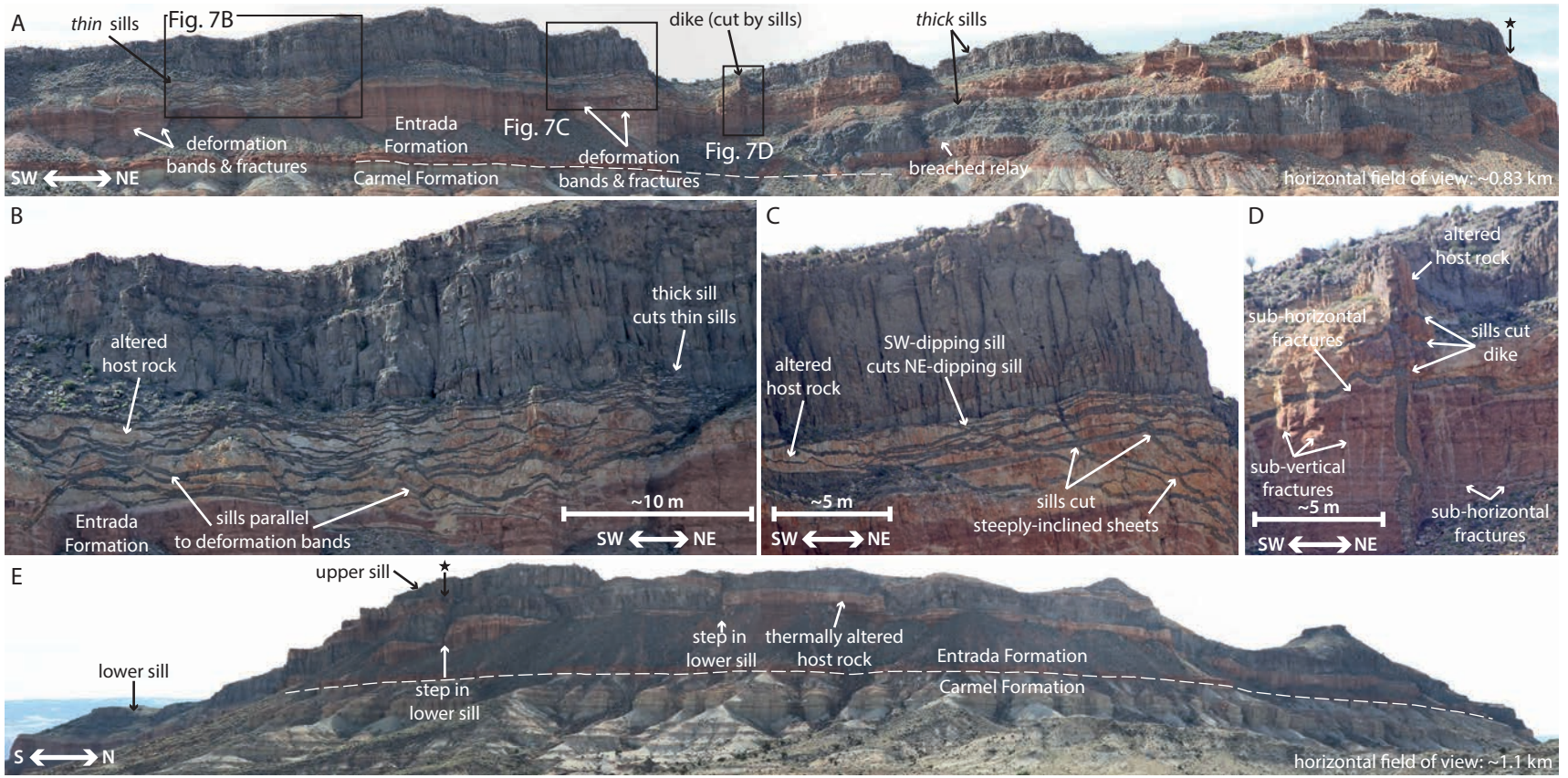

Fig. 7. Examples of sills in the SRSVF. (A) 30 m thick sills in the southern SRSVF, are gently inclined relative to the host stratigraphy (at ~3°) such that the upper sill is observed intersecting the Entrada-Carmel Formation boundary ~700 m to the SW of the photograph. Note right hand edge of A is oriented N-S; black star indicates a marker point linking A and E. Breached relay structures (cf. broken bridges, e.g. Hutton, 2009), which record early sill segments, consistently strike NW-SE. Star shows reference position for view shown in E. (B) Thin sills (10 cm to 1 m thick) occur in close proximity to thick sills. Some thin sills are parallel to deformation bands, whereas some are horizontal. (C) Intrusions range in dip, from horizontal to ~60°; here, steeply inclined sheets are cut and offset by shallowly-dipping sills. (D) Thin and thick sills cut vertical dike. (E) Lower thick sill shows abrupt vertical steps along exposure, whereas upper thick sill does not, suggesting the lower sill may predate the upper. Note the position of the lower sill base contact relative to the Entrada-Carmel Formation boundary.

Fig. 8
W: 185 mm
H: 83 mm
(Full page width)

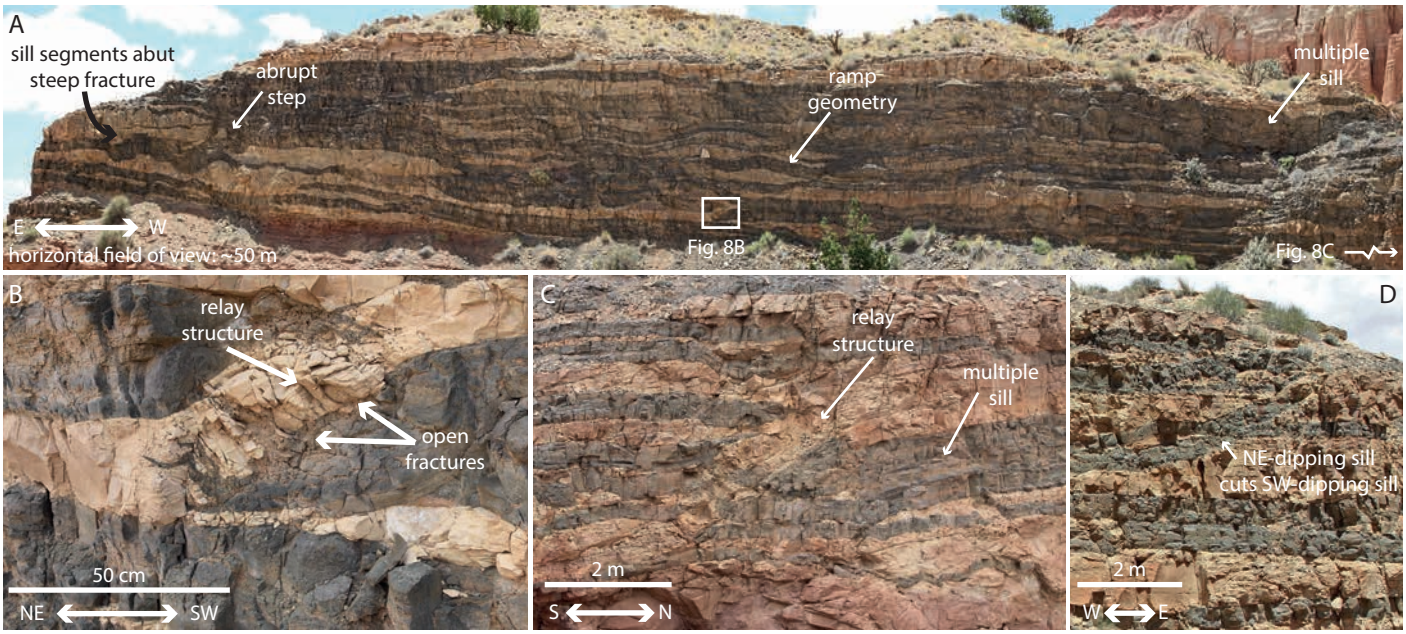

Fig. 8. Examples of thin sills in the SRSVF. (A) Multiple sill network comprising cm-thick sills. Sills are generally bedding parallel but display local ramp sections that dip NE and SW. (B) Some thin sills are segmented, and separated by apparent relay structures that are intruded by inclined sheets. (C) Relay structures occur at a range of scales, up to ~2 m separation. Individual sills are stacked to form a multiple sill. (D) Locally, sills cross-cut each other, indicating staged intrusion.

Fig. 9
W: 185 mm
H: 122 mm
(full page width)

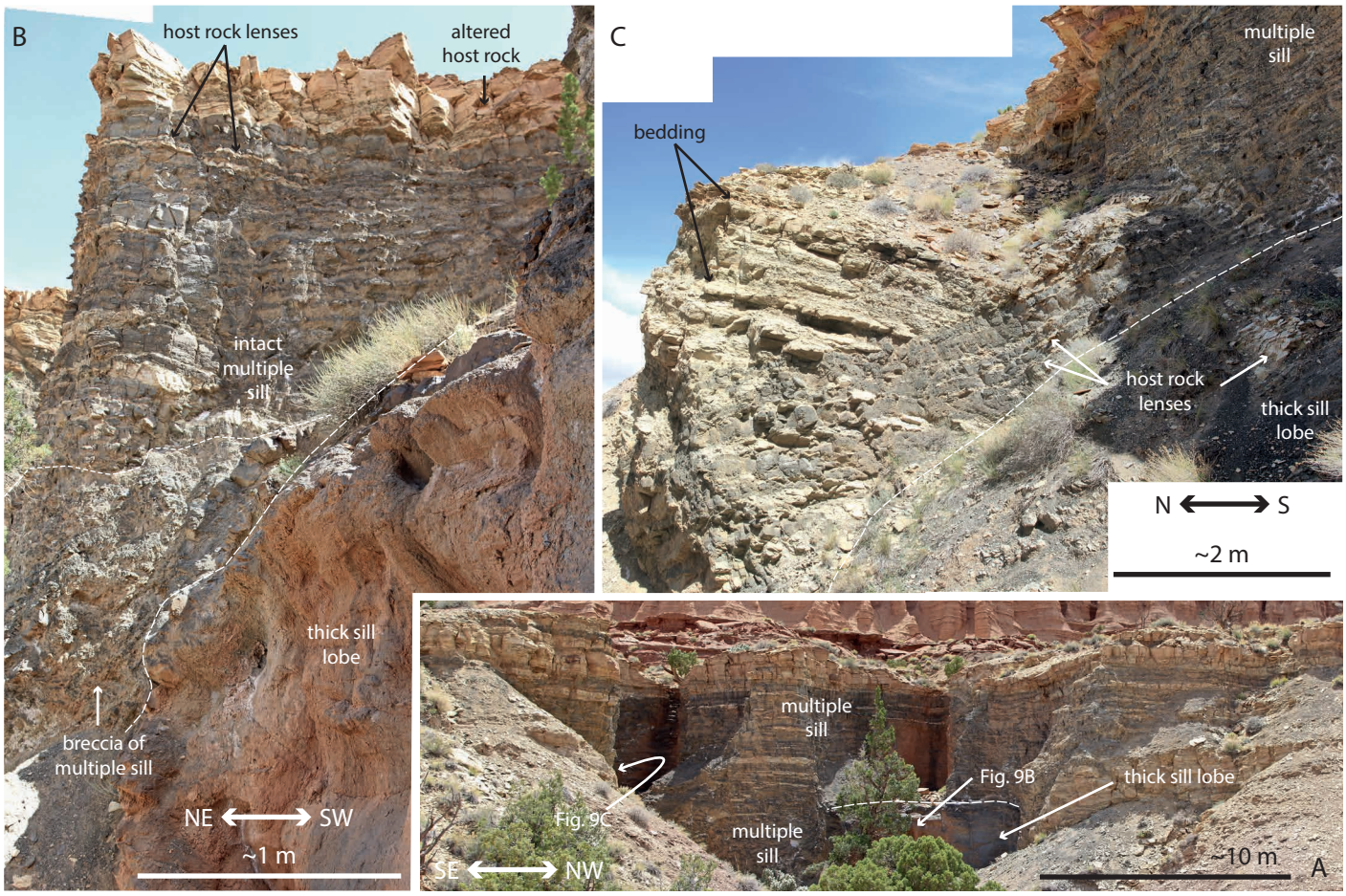

Fig. 9. Relationship between thin and thick sills. (A) Thin sills are stacked to form multiple sills. (B) Locally, thick sill lobes cut thin sill contacts, forming breccia of thin sills. Long-dash line marks the contact between the thick sill and thin sills. Short-dash line marks the boundary between dominantly intact thin sills, and brecciated thin sills. (C) The volume of thick sills appears to be accommodated by folding of the country rock, including the thin sills.

Fig. 10
W: 185 mm
H: 139 mm
(Full page width)

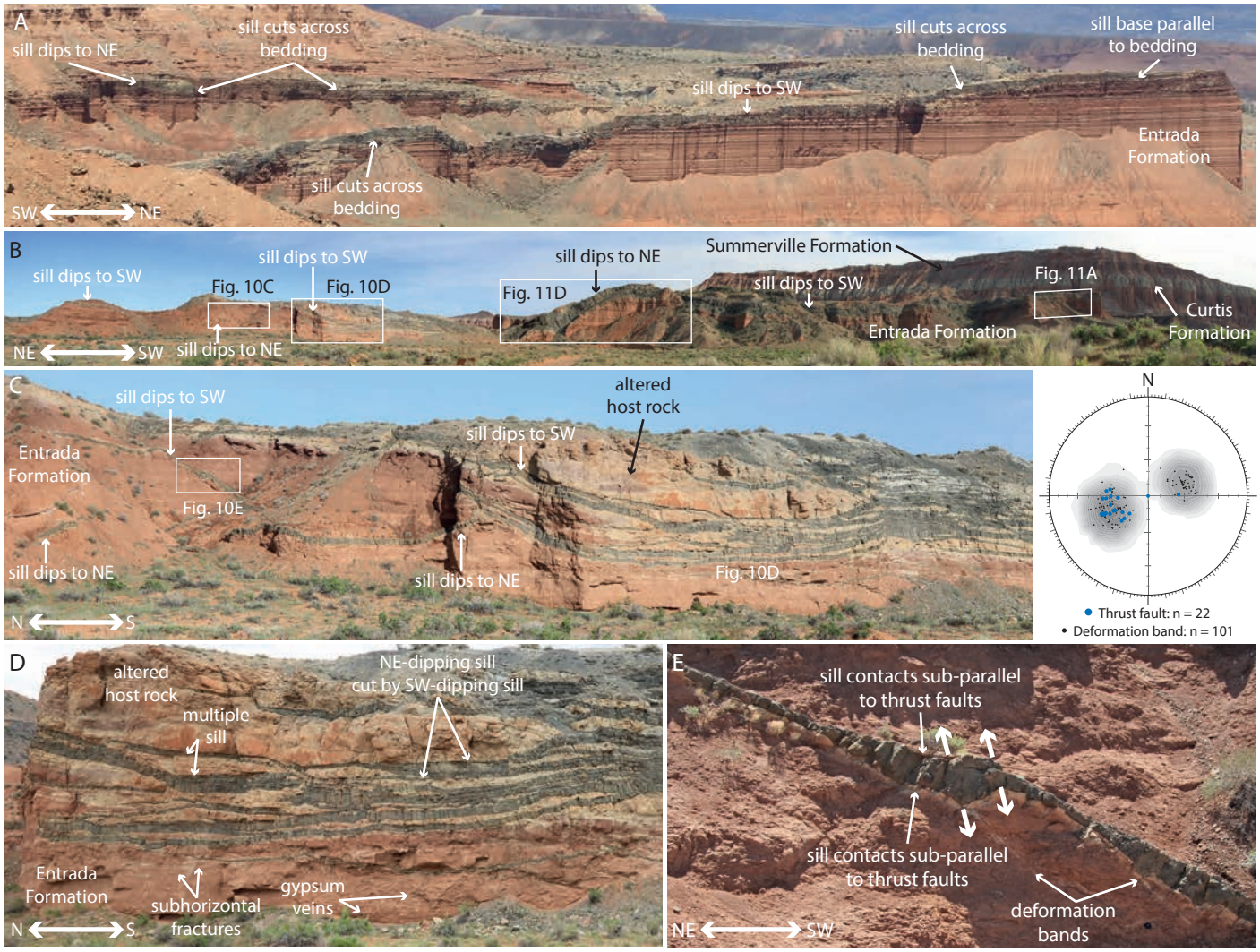

Fig. 10. Gently-dipping sills in the southern SRSVF. (A) Thick sills are locally parallel to host bedding, but otherwise gently climb through the stratigraphy. Sills dips are dominantly NE and SW, and form an acute angle about the horizontal plane. (B) Thick and thin sills show NE and SW dips. (C-D) Thin sills range in attitude from horizontal, to inclined (~20-25°). Lower hemisphere stereographic projection shows deformation bands and thrusts in the southern SRSVF. Sills are locally parallel to (D) bedding, and (E) deformation bands and thrust faults. Thick arrows in E show sill opening direction. Lower hemisphere stereographic projection shows poles to planes for thrust and deformation band data collected in the southern SRSVF, at localities shown in Fig. 10 and Fig. 11. Deformation band data is contoured in grey.

Fig. 11
W: 123 mm
H: 311 mm
(full page width; split to 2 pages for height)

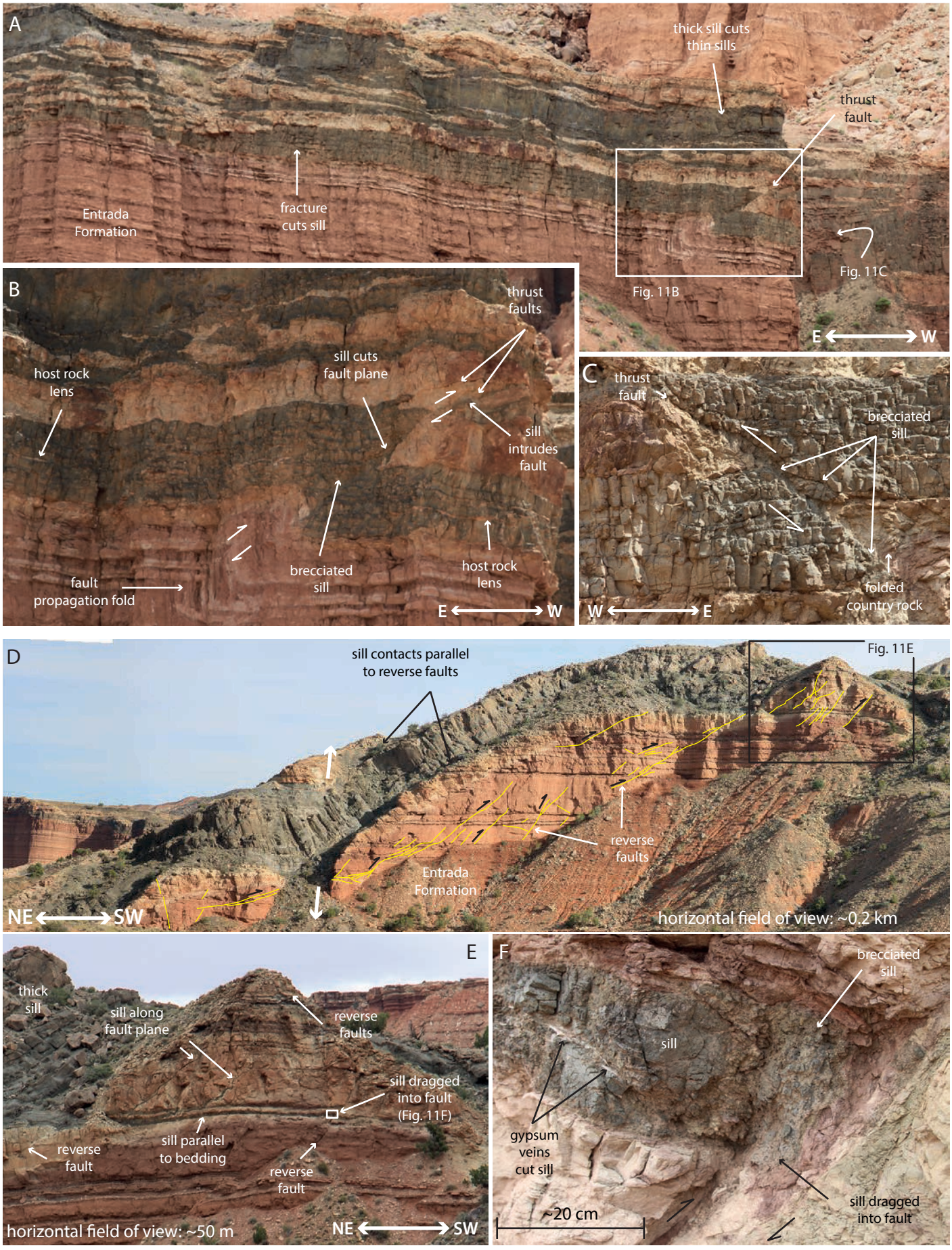

Fig. 11
continued
(full page width)

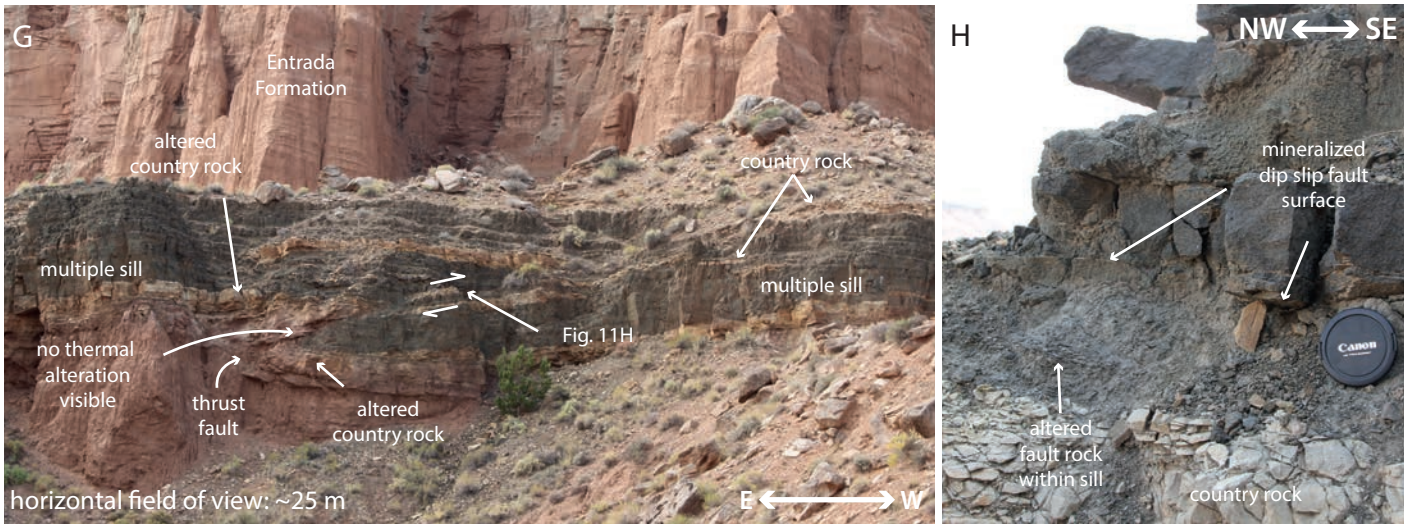

Fig. 11. Relationship between sills and reverse faults. (A-C) Sills cut and are cut by a thrust fault. (B) A multiple sill is cut by an E-dipping thrust. In the upper right of the image, a separate thin sill is observed along the fault plane, inferred as representing post fault intrusion. (C) View from the other side of the crag shown in A and B. Minor fractures parallel to the thrust are observed in the multiple sill. Breccia of the sill is developed along the main thrust, and along minor faults that are sub-parallel to it. (D-F) A thick sill that shows a ramp-flat-ramp geometry, parallel to reverse faults (dipping 25-45° NE) within the country rock. (E-F) Inclined sills appear to have intruded parallel to thrusts, suggesting they reactivate existing structure, but are also locally cut by thrusts. (F) Bedding-parallel sill is dragged into a reverse fault. The sill hosts gypsum-mineralized fractures. Fault rock along the reverse fault comprises breccia of the country rock and the sill. (G) Multiple sill appears to be offset across a thrust fault (dipping ~10°E). Note that the country rock in contact with the sill displays thermal alteration, with the exception of the zone along the thrust plane. (H) Along the fault plane, the sill displays mineralized dip slip fault surfaces, and a 5-10 cm thick zone of altered fault rock.

Fig. 12
W: 123 mm
H: 64 mm
(2-column width)

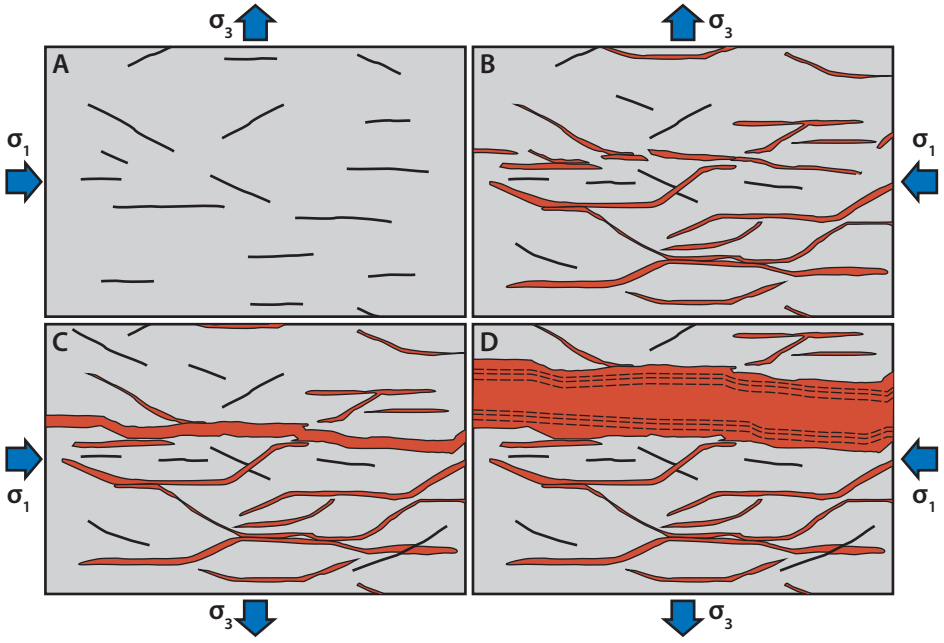

Fig. 12. Conceptual model for sill emplacement during compression. (A) Horizontal shortening produces a fault and fracture system comprising isolated inclined and flat segments. (B) Existing fractures are infilled and inflated by magma and propagate as extension and extensional shear veins. (C) Adjacent sheets link to form a through-going sill. New fractures and faults continue to form during ongoing compression. (D) Minor sills are abandoned in favour of the more thermally -efficient main sill. Note that, as this process may operate across scales, the illustrated box widths may represent centimetres to hundreds of metres, provided there is fault/fracture connectivity in or out of the page.

Fig. 13
W: 123 mm
H: 119 mm
(2-column width)

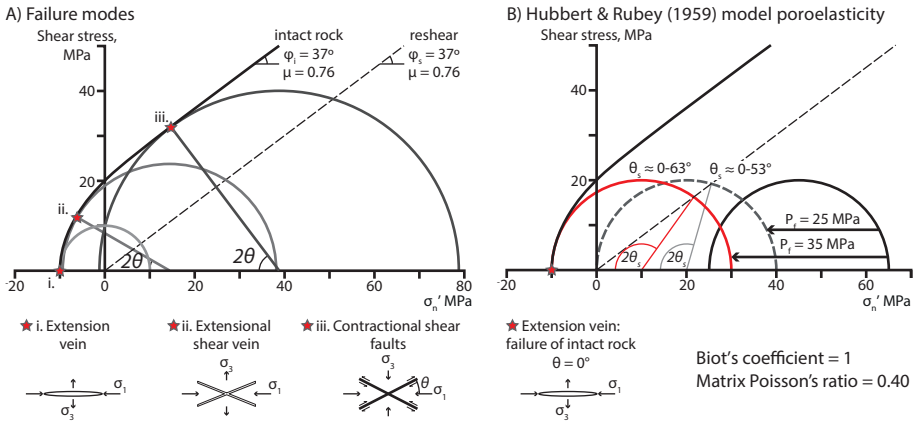

Fig. 13. Mohr diagrams depicting the poroelastic response to isotropic pores and oriented cracks, and to different values of host rock Poisson's ratio. (A) Example Mohr diagram (shear stress, τ, against normal stress, σ) showing the composite failure envelope for intact rock (solid black line) plus the reshear condition for a cohesionless fault (dashed black line), and critical stress circles for the three mesoscopic modes of failure. Diagrams are symmetric about the abscissa, hence the diagrams are simplified to the upper half here. θ represents the angle between the failure plane and the σ1 axis; θs denotes the angular range where reactivation is possible; μ is the coefficient of friction; ϕi is the angle of internal friction for intact rock; ϕs is the angle of internal friction for reshear of a cohesionless fault. Values are idealised based on the Berea sandstone (Healy, 2012). (B) The classical model for the application of fluid pressure (P_f) (after Hubbert and Rubey, 1959). The model involves idealised values for rock compressibility (i.e. Poisson's ratio) and Biot's coefficient, so that the applied fluid pressure has a 1:1 influence on the normal stress.

Fig. 14
W: 123 mm
H: 51 mm
(2-column width)

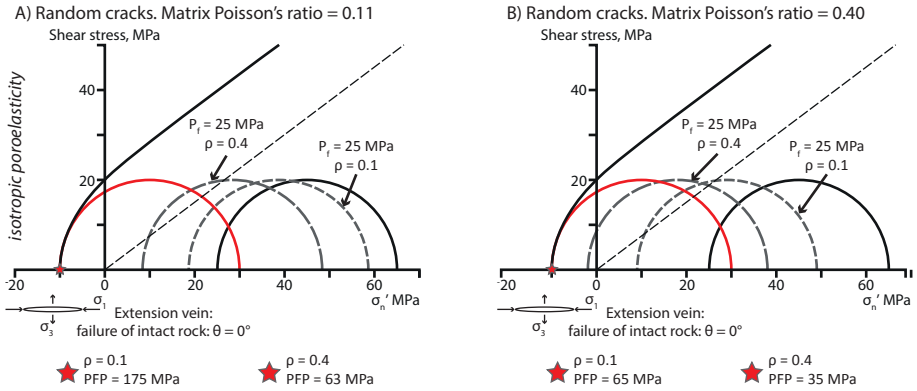

Fig. 14. Mohr diagrams illustrating the poroelastic effect of crack density, and Poisson's ratio at (A) 0.11, and (B) 0.4. Cracks in the model are randomly oriented (i.e. isotropic). Black circles are the normal stress before fluid pressure is applied; grey short-dashed circle shows the effect of 25 MPa fluid pressure where ρ = 0.1; grey long dashed lines circle shows the effect of 25 MPa fluid pressure where ρ = 0.4; red circle shows failure condition.

Fig. 15
W: 123 mm
H: 120 mm
(2-column width)

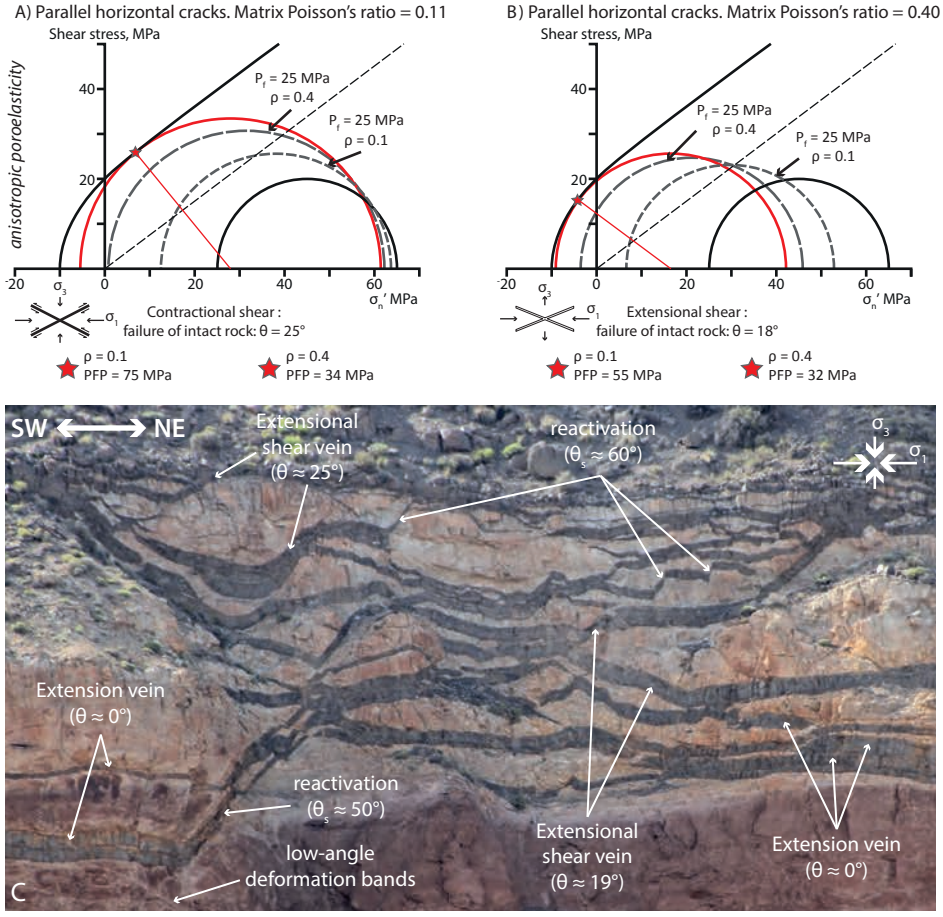

Fig. 15. Mohr diagrams illustrating the poroelastic effect of anisotropic crack density, and Poisson's ratio at (A) 0.11, and (B) 0.4. Cracks in the models are horizontal. Black circles are the normal stress before fluid pressure is applied; grey short-dashed circle shows the effect of 25 MPa fluid pressure where ρ = 0.1; grey long dashed lines circle shows the effect of 25 MPa fluid pressure where ρ = 0.4; red circle shows failure condition. (C) Photograph shows example of sills in the southern SRSVF, highlighting the range of sill attitudes observed in the field. Notably the extension direction is ubiquitously vertical, parallel to our inferred σ_3 axis.